PHYSICAL REVIEW B **104**, 045416 (2021)

Topological metal phases in irradiated graphene sandwiched by asymmetric ferromagnets

Yafang Xu,[1,*] Junshu Ma,[1] and Guojun Jin[2,3,†]
[1]*College of Physics Science and Technology, Yangzhou University, Yangzhou 225002, China*
[2]*School of Physics Science and Technology, Kunming University, Kunming 650214, China*
[3]*National Laboratory of Solid State Microstructures, Department of Physics, and Collaborative Innovation Center of Advanced Microstructures, Nanjing University, Nanjing 210093, China*

(Received 29 January 2021; revised 7 June 2021; accepted 7 July 2021; published 19 July 2021)

The ill-defined Chern number and disappearing topological edge states make it difficult to characterize the topological properties of a metal. In this work, we investigate the abundant topological phases of monolayer graphene, which is sandwiched by asymmetric ferromagnets and irradiated by off-resonant light. In this system, there exist some rarely noticed metal phases, which are spin-valley polarized metal, topological spin metal (TSM), spin half metal, and topological spin half metal (TSHM). Particularly, for the TSM, the subband with spin up or spin down is topological, but the whole state becomes a metal. For the TSHM, a subband with one spin is topological, while the other subband with the opposite spin is insulated, and the whole state is a spin half metal. As a consequence, one topological protected spin current flows on the edge and the other spin propagates in the bulk. Further calculations indicate that the Berry curvatures for the metal phases are nonzero. We propose to probe the topological properties of the metal states with the anomalous Nernst effect. For these topological phases, spin and valley splitting and flip can be obtained by modulating the Fermi level. An electrically or magnetically controlled switch is designed by a two-terminal TSHM junction. It is expected that these topological metal phases can broaden the band engineering in monolayer graphene and support a promising platform for the studies of spin and valley caloritronics.

DOI: 10.1103/PhysRevB.104.045416

I. INTRODUCTION

Since the first fabrication of monolayer graphene in 2004, there have been endless investigations focused on Dirac electrons [1,2]. The results cover topics from mechanics, transport, etc., to topology in both theory and experiment [3–6]. In particular, the novel electronic properties in graphene have promoted the development of other low-dimensional materials such as heavy group-IV monolayers, molybdenum disulfide, and van der Waals heterojunctions composed of different materials [7–12]. Except for modern electronics and spintronics [13,14], the valley degree of freedom in graphene has resulted in a new discipline, i.e., valleytronics [15,16]. For a long time, due to the very tiny spin-orbit coupling strength, which is about 10^{-3} meV, the topological properties in graphene have been difficult to observe. Most research on external field modulated topological phases has concentrated on graphenelike materials, such as silicene, germanene, and stanene, which have sizable spin-orbit couplings of about 3.9, 43, and 100 meV, respectively [10,17–19]. How to realize abundant topological phases in monolayer graphene remains an interesting topic.

For the topological phases of two-dimensional materials, the most familiar and attractive topological states are quantum spin Hall (QSH) phases, quantum valley Hall (QVH) phases, and the quantum anomalous Hall (QAH) phase [3,10,17–20]. The most common methods to characterize these topological phases are to either find the edge states in nanoribbons or calculate the Chern numbers of these systems [21,22]. However, for the metal state, there are no topological edge states and the Chern number is ill defined. Whether a metal state has topological properties is usually ignored, and how to characterize a topological metal state seems difficult. It has been known that the transverse current, which is related to the Berry curvature, is also a sign of a topological transition [23–25]. In addition, the intrinsic multidegrees of freedom in graphene, including charge, spin, and valley, contribute to many fascinating phenomena, such as the bipolar spin-valley diode effect, spin and valley Seebeck effect, etc. [26–28]. How to conveniently control these degrees of freedom and design applications in quantum information and low consumption circuits are still challenging issues [29].

In this work, we investigate the topological phases and peculiar spin- and valley-dependent anomalous thermoelectric transport properties of monolayer graphene, which is sandwiched by asymmetric ferromagnets and irradiated by an off-resonant light. In the process of band evolution by external parameters, a controllable phase diagram is presented. There exist abundant topological phases, such as spin-valley polarized metal (SVPM), topological spin metal (TSM), spin half metal (SHM), topological spin half metal (TSHM), and quantum valley Hall–quantum anomalous Hall insulator (QVH-QAHI), which are special and rarely researched in monolayer graphene. For the TSM, the two subbands with

---

[*] Corresponding author: yfxu@yzu.edu.cn
[†] Corresponding author: gjin@nju.edu.cn

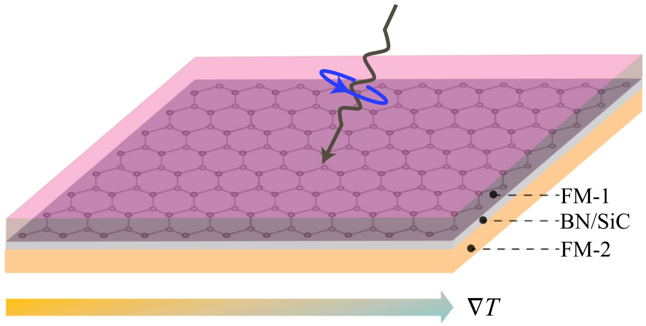

FIG. 1. Schematic of our proposed model, where the graphene monolayer on a BN/SiC substrate is irradiated by an off-resonant light and sandwiched by two asymmetric ferromagnetic layers (FM-1 and FM-2). A temperature gradient $\boldsymbol{\nabla} T$ is applied along the x direction.

opposite spins are all topological, but the bulk state is a metal. For the TSHM, a subband with one spin is topological, but the other subband with the opposite spin is insulated, and the bulk state of the whole band is a spin half metal. More different, when the Fermi level lies in the gap of one spin subband, the currents with different spins are separated spatially. Moreover, it is found that although the edge states and Chern number can only poorly characterize the topological metal and half metal, the Berry curvatures are still nonzero. We further investigate the anomalous Nernst effect under the modulation of the Fermi level. The deflection of the Nernst current is dependent on the Berry curvature and the index of the conduction or valence band. Taking advantage of the various topological phases, the spin and valley splitting, spin flip, and electrically or magnetically controlled on-off switch can be flexibly realized.

The paper is organized as follows. In Sec. II, we construct the model and introduce the system Hamiltonian. In Sec. III, we present the phase diagram, determine the phase boundaries, and concentrate on several particular topological metal phases. In Sec. IV, we consider the Berry curvature and anomalous thermoelectric transport properties. In Sec. V, a possible application about the topological phase in spin and valley caloritronics is designed. Finally, in Sec. VI, a summary is given of the whole work.

II. MODEL HAMILTONIAN

We consider an epitaxial monolayer graphene in the xy plane; a schematic is shown in Fig. 1. Under the modulation of external fields, including the substrate potential, light irradiation, and magnetic interaction, the tight-binding Hamiltonian of monolayer graphene is written as

$$\mathcal{H} = -t \sum_{\langle m,n\rangle\sigma} c^{\dagger}_{m\sigma} c_{n\sigma} + \lambda_z \sum_{m\sigma} \mu_m c^{\dagger}_{m\sigma} c_{m\sigma} + i\frac{\lambda_\Omega}{3\sqrt{3}} \sum_{\langle\langle m,n\rangle\rangle\sigma} \sigma \nu_{mn} c^{\dagger}_{m\sigma} c_{n\sigma} + M \sum_{m\sigma} c^{\dagger}_{m\sigma} \tau_\chi \sigma_z c_{m\sigma}, \quad (1)$$

where the operator $c^{\dagger}_{m\sigma}$ ($c_{m\sigma}$) represents the creation (annihilation) of one electron with spin σ at site m, and $\langle m, n\rangle$ and $\langle\langle m, n\rangle\rangle$ run over all the nearest- and next-nearest-neighbor hopping sites, respectively. In Eq. (1), the first term is the nearest-neighbor hopping with the hopping energy $t = 2.97$ eV. The second term is the staggered sublattice potential, which can be induced by a hexagonal boron nitride (hBN) or SiC substrate. It should be noted that due to the 1.8% mismatch of lattice constants between graphene and hBN, a long wavelength moiré pattern can appear in a large size. Considering the finite size of graphene nanoribbons and the low-energy transport at the Dirac cones, the zero relative rotation is assumed and lattice mismatch is neglected. In experiment, it has been realized that graphene can align with the underlying hBN lattice within an error of less than 0.05° [30,31]. $\mu_m = \pm 1$ indicates that the site m lies on the A or B sublattices. The third term is the Haldane term, which can be induced by the off-resonant irradiation [19,25,32]. The irradiation parameter $\lambda_\Omega = \xi e^2 A^2 v_{\mathrm{F}}^2/\hbar\Omega$ with e the electron charge, A the amplitude, Ω the frequency of the light, and $\xi = +1(-1)$ the right (left) circulation of light. $\nu_{mn} = +1(-1)$ represents that the next-nearest-neighbor hopping is anticlockwise (clockwise). The fourth term represents the exchange magnetization coming from two asymmetric ferromagnets, and the monolayer graphene is intercalated between them [27,33]. Some experimental proposals indicate that the ferromagnetic Co/Ni or the EuS and YIG films can be used as good candidates [34–36]. Except for the sandwiched structure, another method of absorbing two different transition metals to the A and B sublattices is also proposed to realize the exchange fields [17]. M is the strength of the exchange field. σ_z is the z component of the Pauli matrix in spin subspace. The 2×2 matrix τ_χ describes the asymmetry of the ferromagnets. It can be written as

$$\tau_\chi = \begin{pmatrix} 1 & 0 \\ 0 & \chi \end{pmatrix}. \quad (2)$$

When $\chi = 1(-1)$, it is a ferromagnetic (antiferromagnetic) exchange field. Otherwise, it is mixed by both cases.

The next-nearest-neighbor tight-binding model is usually used to calculate the band structure of a nanoribbon and to exhibit the edge states. In order to further analyze the physics of the electronic behavior near the Dirac cones, the effective four-band low-energy Hamiltonian can be written as

$$\mathcal{H} = \hbar v_{\mathrm{F}}(\eta\tau_x k_x + \tau_y k_y) + \lambda_z \tau_z + \eta\lambda_\Omega \tau_z + M\tau_\chi \sigma_z, \quad (3)$$

where $v_{\mathrm{F}} = 10^6$ m/s is the Fermi velocity of graphene, and $\hbar v_{\mathrm{F}} = \sqrt{3}at/2$, with a the lattice constant, $\tau_{x,y,z}$ and σ_z are the Pauli matrices of the sublattice pseudospin and real spin, $\boldsymbol{k} = (k_x, k_y)$ is the wave vector, and $\eta = 1(-1)$ denotes the index of the $K(K')$ valley.

By solving the Schrödinger equation, eight spin- and valley-dependent bands in the energy spectrum can be obtained as

$$E_n(k) = \frac{1}{2}\left[\sigma M(1+\chi) + n\sqrt{\Delta^2_{\sigma,\eta} + 4\hbar^2 v_{\mathrm{F}}^2 k^2}\right], \quad (4)$$

where $n = +(-)$ denotes the conduction(valence) band, and $\sigma = +(-)$ denotes spin up (spin down). The term $\Delta_{\sigma,\eta}$ can be viewed as the spin- and valley-dependent band gap at the Dirac cone, which is given as

$$\Delta_{\sigma,\eta} = \sigma M(1-\chi) + 2(\lambda_z + \eta\lambda_\Omega). \quad (5)$$

For each spin-resolved subband, the size of the band gap is given by $|\Delta_{\sigma,\eta}|$. It is located at the K and K' valleys and closed when $\Delta_{\sigma,\eta} = 0$. However, for the whole energy band, the conductive property depends on Eq. (4), where the term $M(1+\chi)$ breaks the electron-hole symmetry of each spin subband.

Before proceeding with the above results, we should present a more detailed description of the off-resonant light. When the light frequency is off resonant, it does not excite electrons directly and instead modifies the band structure effectively by virtual photon processes. The off-resonant condition requires that the frequency is high, and $\hbar\Omega \gg t$. Compared with the effective Hamiltonian of a periodically driven system in the Brillouin-Wigner expansion, the strength of the next-nearest-neighbor hopping term should written as $-\frac{\tilde{t}^2}{\Omega}\sum_{n\neq 0}\frac{\mathcal{J}_n^2(\mathcal{A})}{n}\sin\frac{2\pi n}{3}$, where $\tilde{t} = t\mathcal{J}_0(\mathcal{A})$ is the renormalized hopping energy, $\mathcal{J}_n(\mathcal{A})$ is the nth Bessel function of the first kind, and $\mathcal{A} = eaA/\hbar$ is a dimensionless number [37]. It describes the multiphoton processes. In the weak field and high-frequency regime, it just corresponds to the single-photon process ($n = 1$) proposed by Kitagawa *et al.*, and the higher-order terms are suppressed by $\mathcal{A}^2$ [32]. To simplify, in our model we consider the low-intensity limit, $\mathcal{A}^2 \ll 1$. The effective Hamiltonian of off-resonant light in this case is simply the Hamiltonian proposed by Haldane [32,38].

In addition, it can be understood that the effective mass term from the exchange field M and inversion symmetry breaking term λ_z actually should be renormalized under an off-resonant electromagnetic field [39]. In the case of high-frequency light irradiation, the effective band gap can be renormalized into

$$\tilde{\Delta}_{\sigma,\eta} = \frac{\sigma M(1-\chi)+2\lambda_z}{\sqrt{1+\left(\frac{2ev_{\rm F}A}{\hbar\Omega}\right)^2}} + \eta\xi\hbar\Omega\left[\sqrt{1+\left(\frac{2ev_{\rm F}A}{\hbar\Omega}\right)^2}-1\right], \tag{6}$$

where the first term comes from the exchange field and staggered potential, and the second term is a light-induced band gap. $1/\sqrt{1+(2ev_{\rm F}A/\hbar\Omega)^2}$ can be viewed as the renormalized factor of the exchange field and staggered potential. Compared with Eq. (5), when $(2ev_{\rm F}A/\hbar\Omega)^2$ is much less than 1, i.e., the laser light has low amplitude and high frequency, the band gap can be approximated by $\tilde{\Delta}_{\sigma,\eta} = \Delta_{\sigma,\eta}$. For the sake of the requirement of off-resonant light in graphene, the frequency needs to satisfy $\hbar\Omega \gg t$, and the frequency is not less than 3500 THz. If we adopt the lowest frequency $\Omega \approx$ 3500 THz in the soft x-ray regime, the amplitude of the vector potential $A = 2.4 \times 10^3$ V s/m, the gap induced by the off-resonant light can reach about 50 meV, and $(2ev_{\rm F}A/\hbar\Omega)^2 \approx 0.04$ is smaller than 1 by about two orders of magnitude. Hence, the renormalized effect on the exchange field and staggered potential is ignored in our case. From Eq. (6), we can find that if the term $ev_{\rm F}A/\hbar\Omega$ is large, the effective mass term from the exchange field and staggered potential becomes small, the light field plays the main role, and some topological metal phases will disappear. For exhibiting the abundant topological phases, we choose the approximation $\mathcal{A}^2 \ll 1$ and high frequency $\hbar\Omega \gg t$ for the off-resonant light. In this approximation, we obtain the Hamiltonian of Eqs. (1) and (3), where the exchange field and inversion symmetry breaking term are not affected by the light.

III. PHASE DIAGRAMS AND TOPOLOGICAL PHASES

By applying different fields to monolayer graphene, various topological phases are found, and the phase diagrams in the λ_Ω-M plane are summarized in Fig. 2. We fix the staggered potential $\lambda_z = 0.1$ eV, and tune the irradiation parameter λ_Ω and exchange-field strength M in three different cases: $\chi = 1$, $\chi = 0$, and $\chi = -1$. For actual parameters of the staggered potential, previous investigations show that a band gap about 53 meV can be opened in graphene on hBN [40,41]. When graphene is epitaxially grown on a SiC substrate, a band gap of about 0.26 eV can be reached [42]. Edge states can be clearly shown in the energy structure, when the staggered potential is reasonably chosen as $\lambda_z = 0.1$ eV. It can be verified that if we reduce the staggered potential and modulate other external fields correspondingly, the phase diagrams are maintained. The heavy lines in the phase diagrams are the phase boundaries, which could be derived based on the low-energy Dirac theory.

Considering the topological properties, the phase boundaries are partly determined by the spin-resolved subband gap. They are given as

$$M(1-\chi) + 2\sigma(\lambda_z + \eta\lambda_\Omega) = 0. \tag{7}$$

For the bulk state, when the band gaps from the same valley but different spins are closed, an insulating and metallic phase transition occurs. The phase boundaries depend on the equation, which can be analytically written as

$$M(1+\chi) + 2\sigma(\lambda_z + \eta\lambda_\Omega) = 0. \tag{8}$$

In addition, if the conduction and valence bands from different valleys are mixed, the metal state can also appear, and the boundaries are given as

$$M(1+\sigma) + M\chi(\sigma-1) = -2\sigma\lambda_z$$

$$\text{if}\quad \Delta_{\sigma,1} \geqslant 0 \quad\text{and}\quad \Delta_{-\sigma,-1} \geqslant 0, \tag{9a}$$

$$M(\sigma-1) + M\chi(\sigma+1) = 2\sigma\lambda_z$$

$$\text{if}\quad \Delta_{\sigma,1} \leqslant 0 \quad\text{and}\quad \Delta_{-\sigma,-1} \leqslant 0, \tag{9b}$$

$$M(1+\chi) = -2\lambda_\Omega$$

$$\text{if}\quad \Delta_{\sigma,1} \geqslant 0 \quad\text{and}\quad \Delta_{-\sigma,-1} \leqslant 0, \tag{9c}$$

$$M(1+\chi) = 2\lambda_\Omega$$

$$\text{if}\quad \Delta_{\sigma,1} \leqslant 0 \quad\text{and}\quad \Delta_{-\sigma,-1} \geqslant 0. \tag{9d}$$

It could be noted that when $\chi = 0$, the dashed lines $M = \pm 2\lambda_z$ in the purple region of Fig. 2 distinguish the valley-locked TSHM and valley-mixed TSHM. Between the two lines, they are the valley-locked TSHMs. Above $M = 2\lambda_z$ and below $M = -2\lambda_z$, they are the valley-mixed TSHMs.

To show the topological phases, some typical band structures of graphene nanoribbons with zigzag edges are shown in Fig. 3, where the band structures in Figs. 3(a) to 3(i) correspond to the marked points in Fig. 2. The characteristics of the various topological phases are summarized in Table I. For a topological insulator, the spin- and valley-dependent Chern

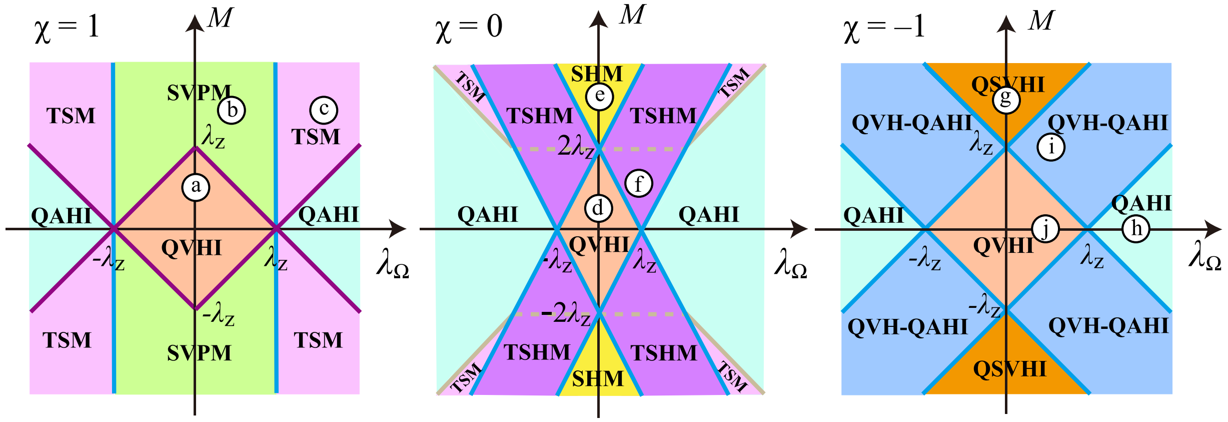

FIG. 2. The phase diagrams with different χ in the λ_Ω-M plane. The staggered potential λ_z is fixed as 0.1 eV. The heavy lines denote the phase boundaries.

number $\mathcal{C}_{\sigma,\eta}$ can be derived as

$$\mathcal{C}_{\sigma,\eta} = -\frac{\eta}{2}\mathrm{sgn}(\Delta_{\sigma,\eta}). \tag{10}$$

Four independent Chern numbers are used to characterize the topological phases, which are the charge Chern number $\mathcal{C}_\mathrm{c}$, spin Chern number $\mathcal{C}_\mathrm{s}$, valley Chern number $\mathcal{C}_\mathrm{v}$, and spin-valley Chern number $\mathcal{C}_\mathrm{sv}$. They can be defined as $\mathcal{C}_\mathrm{c} = \sum_{\sigma,\eta}\mathcal{C}_{\sigma,\eta}$, $\mathcal{C}_\mathrm{s} = \sum_{\sigma,\eta}\sigma\mathcal{C}_{\sigma,\eta}$, $\mathcal{C}_\mathrm{v} = \sum_{\sigma,\eta}\eta\mathcal{C}_{\sigma,\eta}$, and $\mathcal{C}_\mathrm{sv} = \sum_{\sigma,\eta}\sigma\eta\mathcal{C}_{\sigma,\eta}$, respectively.

For Figs. 3(a) and 3(d), they are quantum valley Hall insulators (QVHIs) [17,18], whose Chern numbers are $[0, 0, -2, 0]$. In these phases, the staggered potential λ_z, which breaks the inversion symmetry, plays a significant role on the QVHI. In order to check the effect of the staggered potential on the QVHI clearly, we plot the band structures when $\lambda_z = 0$ in Fig. 4 as a contrast. Comparing their band structures, the QVHI phases are violated and turn into the SVPM, SHM, and QAHI, respectively. Differently, the spin polarization is modulated by χ. When the Fermi level lies in the gap, neither edge nor bulk currents appears, but a transverse valley current exists. Compared with the quantum spin-valley Hall insulator (QSVHI) in Fig. 3(g), whose Chern numbers are $[0, 0, 0, -2]$, although the band structures are similar, the spin- and valley-dependent transverse currents are different. The QSVHI has not been extensively investigated in monolayer graphene, but the topological properties are akin to those in silicene [17]. In the right and left (the parts with pale-turquoise color) of each phase diagram in Fig. 2, the off-resonant light plays the main role; they are the QAHIs with the Chern numbers being $[-2, 0, 0, 0]$ [19,25]. It can be seen from Fig. 3(h) that topological edge states exist. For Figs. 3(b) and 3(c), from their bulk band structures, both are a SVPM state. However, with regard to the latter, the bands for each spin are a topological insulator, which is called the TSM state. When $\chi = 0$, it is a critical case. The subband of one spin is in contact with the subband of the opposite spin, and the gap is closed. As shown in Figs. 3(e) and 3(f), they are SHM and TSHM. Different from the traditional half

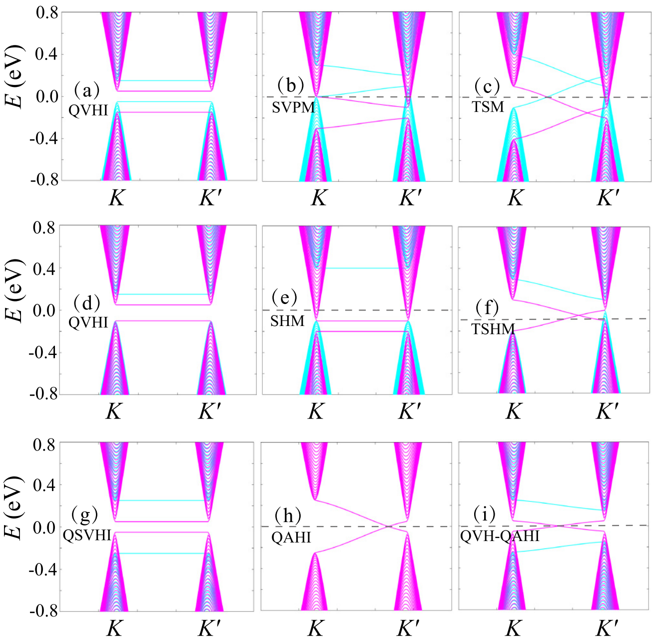

FIG. 3. The band structures of a zigzag graphene nanoribbon in different external fields corresponding to the points (a)–(i) labeled in the phase diagrams of Fig. 2. The width of the nanoribbon is 512 atoms. The blue (fuchsia) color denotes spin up (down).

TABLE I. Topological phases and their characteristics. Yes (No) means that the corresponding topological phase has (has not) been mentioned before.

Topological phases	Chern numbers $[\mathcal{C}_\mathrm{c}, \mathcal{C}_\mathrm{s}, \mathcal{C}_\mathrm{v}, \mathcal{C}_\mathrm{sv}]$	Edge and/or bulk state	Silicene	Graphene
QVHI	[0,0,−2,0]	Neither	Yes	Yes
QAHI	[−2,0,0,0]	Edge	Yes	Yes
QSVHI	[0,0,0,−2]	Neither	Yes	No
QVH-QAHI	[−1, −1, 1, −1]	Edge	Yes	No
SVPM	None	Bulk	Yes	No
TSM	None	Bulk	No	No
SHM	None	Bulk	Yes	No
TSHM	None	Both	No	No

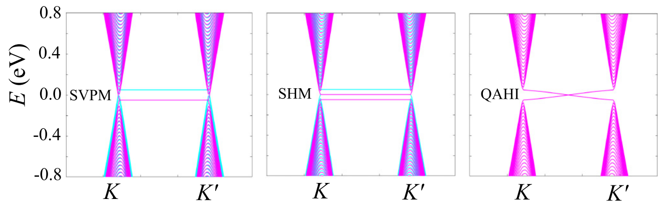

FIG. 4. The band structures of a zigzag graphene nanoribbon when the staggered potential $\lambda_z = 0$. The other parameters in the three subgraphs are the same as those in the QVHI phases in Fig. 2, which are marked by points (a), (d), and (j), respectively.

metal where the gap is closed with the same spin, the gap in spin half metal is closed with different spins [43]. When $\chi = -1$ in Fig. 2, there is no metal state, and all the half metal states when $\chi = 1$ are transited into insulating states. One special state is the QVH-QAHI, whose Chern numbers are $[-1, -1, 1, -1]$. From the band structure in Fig. 3(i), it can be seen that the subband with one spin is a topological insulator, and the subband with the opposite spin is a band insulator. It is different from the edge states in the QAHI of Fig. 3(h), where the subbands with both spins are the QAHIs. For these topological phases, we do a survey to see whether they have been found in monolayer graphene before, and compare the results with those in silicene. It should be noted that although the SVPM and SHM have been mentioned in silicene [18,27], the topological properties and anomalous Nernst transport have not been investigated. Some topological metal states will be impeded by the Rashba spin-orbit coupling [18].

Aiming at some specific cases, we further investigate the edge and bulk modes. The schematics of the edge and bulk states are illustrated in Figs. 5(a)– 5(f), where the directions of the arrows denote the current moving directions. The Fermi levels are marked in Figs. 3(b), 3(c), 3(e)–3(g), and 3(i). For the SVPM in Fig. 3(b) and TSM in Fig. 3(c), both of the bulk states are valley-polarized metal. Considering the position of the Fermi level, the contributions of the currents are from two valleys for the SVPM, and only the K' valley for the TSM, as shown in Figs. 5(a) and 5(b). The current from the bulk state is completely valley polarized in the TSM. Since the electrons participating in the transport come from the conduction band with spin up and valance band with spin down, the currents with spin up and spin down are reversed, and a pure spin current can be realized. With regard to the SHM in Fig. 3(e), the bulk currents are 100% spin polarized, as shown in Fig. 5(c). When the system lies in the TSHM phase, such as in Fig. 3(f), the subband with spin down is a topological insulator. When the Fermi level is located in the gap, there exist topological edge states with spin down. Hence, the current with spin down flows on the edge; the current with spin up contributes to the bulk transport. The schematic is shown in Fig. 5(d), where the spins are spatially isolated. For the QAHI and QVH-QAHI in Figs. 3(g) and 3(i), when the Fermi level lies in the gap, there is no current from the bulk state and only an edge current appears. For the QAHI, they are chiral and spin degenerate, which is shown in Fig. 5(e). The edge state for QVH-QAHI is completely spin polarized, which can be clearly seen in Fig. 5(f).

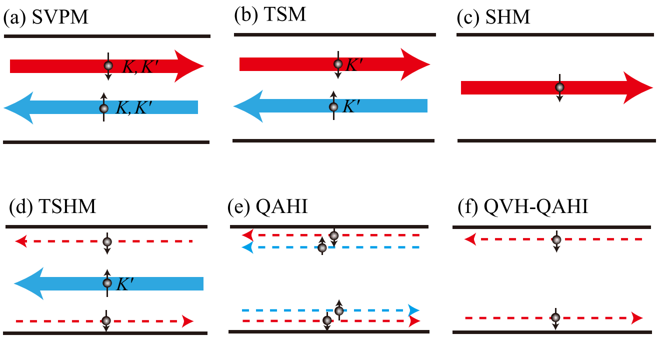

FIG. 5. Schematics of the edge and bulk states for some special phases corresponding to those in Figs. 3(b), 3(c) 3(e)–3(g), and 3(i). The thick solid arrows represent the currents flowing in the bulk, while the thin dashed arrows represent the edge states propagating at the edge. The arrows labeled on the balls denote the spin up and down.

IV. BERRY CURVATURE AND ANOMALOUS NERNST EFFECT

For topological insulators, the topological Chern numbers (C_c, C_s, C_v, C_{sv}) or edge states can be used to characterize them. However, because of no gap in the metal state, the Chern number is ill defined and the edge states disappear. We further study the Berry curvature and anomalous Nernst effect, which can also be viewed as a characteristic of topological properties. Because the spin is a good quantum number in this system, the four normalized spinor wave functions can be written as

$$\Psi_{1,2}(x) = 1/\sqrt{C^2+1}(Ce^{-i\eta\theta}, 0, 1, 0)^{\mathrm{T}} e^{i\boldsymbol{k}\cdot\boldsymbol{r}}, \tag{11a}$$

$$\Psi_{3,4}(x) = 1/\sqrt{C^2+1}(0, Ce^{-i\eta\theta}, 0, 1)^{\mathrm{T}} e^{i\boldsymbol{k}\cdot\boldsymbol{r}}, \tag{11b}$$

where

$$C = \frac{\Delta_{\sigma,\eta} \pm \sqrt{\Delta_{\sigma,\eta}^2 + 4k^2}}{2\eta k}, \tag{12}$$

$\theta = \arctan(k_y/k_x)$ is the azimuthal angle of wave vector $\boldsymbol{k}$, and $\boldsymbol{r} = (x, y)$ is the position vector. It can be seen from the eigenstates in Eqs. (11a) and (11b) that the wave functions depend on the spin- and valley-dependent effective mass $\Delta_{\sigma,\eta}$.

The Berry curvature is defined by $\boldsymbol{\Omega}_n(k) = \boldsymbol{\nabla}_k \times \langle u_n(k)|i\nabla_k|u_n(k)\rangle = \Omega_n(k)\boldsymbol{z}$, where $|u_n(k)\rangle$ is the periodic amplitude of the wave function of the nth band, and $\boldsymbol{z}$ is the unit vector in the perpendicular direction. The Berry curvature can be obtained as

$$\Omega_n(k) = -n\eta \frac{2\hbar^2 v_{\mathrm{F}}^2 \Delta_{\sigma,\eta}}{\left(4\hbar^2 v_{\mathrm{F}}^2 k^2 + \Delta_{\sigma,\eta}^2\right)^{3/2}}. \tag{13}$$

From the above equation, one can find that the Berry curvature also depends on the band gap of the spin-resolved subband, but is robust against the term $\sigma M(1+\chi)$ in Eq. (4), which moves the bands upward or downward.

The Berry curvatures of several topological phases corresponding to Figs. 3(b), 3(c) 3(e), 3(f), and 3(i) are shown in Fig. 6. Obviously, even though the system is a metal, the Berry

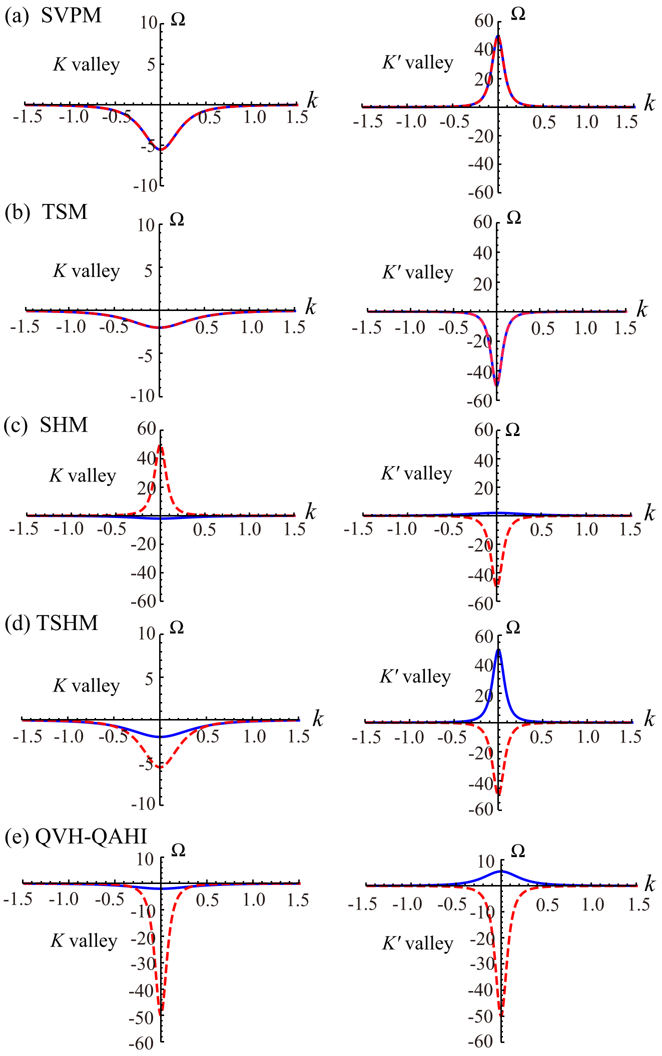

FIG. 6. Berry curvatures of the conduction band electrons for different topological phases. The Berry curvature in the vertical axis is in units of $3a^2/4$; the wave vector in the horizontal axis is in units of $2/\sqrt{3}a$. The parameters in (a)–(e) correspond to those in Figs. 3(b), 3(c) 3(e), 3(f), and 3(i), respectively. The left (right) column represents the Berry curvature of the $K(K')$ valley. The blue solid (red dashed) line denotes the Berry curvature with spin up (down).

curvature is nonzero. For the SVPM and SHM states, the Berry curvatures in different valleys are reversed. For the TSM state, all the Berry curvatures with different valleys and spins are homodromous. For the TSHM state, the Berry curvature with spin up at the K valley is reversed. The finite Berry curvatures in the TSM and TSHM are obviously distinct from conventional metal, where the Berry curvature is zero [20]. For the QVH-QAHI state, the Berry curvatures with same spin at the K and K' valleys have the same sign, while those with opposite spins at different valleys have opposite signs. For same spin, it is a QVHI. For opposite spins, it is a QAHI.

To exhibit the measurable properties, we further investigate the anomalous Nernst effect, where a transverse electric current is generated by applying a longitudinal temperature gradient. It has been known that if a nonzero Berry curvature exists, the group velocity of a Bloch electron will obtain a transverse velocity component, $\dot{\boldsymbol{r}} = \frac{\partial E_n(k)}{\hbar\partial k} + \frac{e}{\hbar}\boldsymbol{E}\times\boldsymbol{\Omega}_n(k)$, where $E_n(k)$ is the nth band energy and $\boldsymbol{E}$ is the external longitudinal electric field [23]. The Berry curvature $\boldsymbol{\Omega}$, which plays an analogous role of a real magnetic field, is the origin of the anomalous Nernst effect. Considering the self-rotation of the wave packet and the topological effect of the Berry curvature, the transverse Nernst current $\boldsymbol{J}_n$ in the presence of a temperature gradient can be written as

$$\boldsymbol{J}_n = -\frac{\nabla T}{T}\sum_n \frac{e}{\hbar}\int \frac{d\boldsymbol{k}}{(2\pi)^2}\Omega_n\{[E_n(k)-E_\mathrm{F}]f_k + k_\mathrm{B}T\ln\left(1+e^{-\frac{E_n(k)-E_\mathrm{F}}{k_\mathrm{B}T}}\right)\}. \tag{14}$$

Here, $f_k = 1/[1+e^{[E_n(k)-E_\mathrm{F}]/k_\mathrm{B}T}]$ is the Fermi distribution function, E_F is the Fermi energy, and the sum is taken over the conduction and valence bands.

According to the relation $\boldsymbol{J}_n = \alpha_n(-\nabla T)$, the anomalous Nernst conductivity can be extracted. After some derivations, it can be written into a more simplified form,

$$\alpha_n = -\frac{ek_\mathrm{B}}{4\hbar\pi^2}\sum_n\int[f_k\ln f_k + (1-f_k)\ln(1-f_k)]\Omega_n d\boldsymbol{k}. \tag{15}$$

In the numerical calculations, we set the temperature $k_\mathrm{B}T = 2.5$ meV, and the unit of the Nernst conductivity is $ek_\mathrm{B}/h = 3.33$ nA/K. We plot the Nernst conductivity in Figs. 7(a)–7(e), which correspond to the five particular topological phases. The irradiated off-resonant light is right circularly polarized. The range of the Fermi level is selected in $[-0.1, 0.1]$ eV. When the energy is larger than the Fermi level by several $k_\mathrm{B}T$, the opportunity of the states contributing to the transport is very small. The electrons near the Fermi level play the main role for the Nernst conductivity.

The spin-valley-dependent and total Nernst conductivities in different topological phases are shown in Fig. 7. The total Nernst conductivity is the sum of all the spin and valley components. In experiment, the total Nernst conductivity can be directly observed by transverse measurement, while the spin- or valley-resolved Nernst currents can be detected by a Hall bar geometry via the inverse spin or valley Hall effect in accordance with the recent experimental results [44–46]. For the SVPM and TSM states, part of the particles contributing to the transport comes from the conduction band with spin down, and the other part comes from the valence band with spin up. It is different from the traditional topological insulator, where the electrons contributing to the transport are from the conduction or valence band simultaneously. Although the bulk states are similar, a remarkable difference exists in the Berry curvature, as can be seen in Figs. 6(a) and 6(b). As a consequence, the Nernst conductivities in the SVPM are spin and valley polarized, while the Nernst conductivities in the TSM with spin down and spin up are reversed, as shown in Figs. 7(a) and 7(b). To be noticed, the total Nernst conductivity in Fig. 7(a) is spin and valley mixed, while in Fig. 7(b), the total Nernst conductivity is 100% valley polarized. The Nernst conductivities in the TSM are from the K' valley. The valley-locked spin splitting is realized. If the system situates in the SHM, the directions of the Berry curvatures in different valleys are

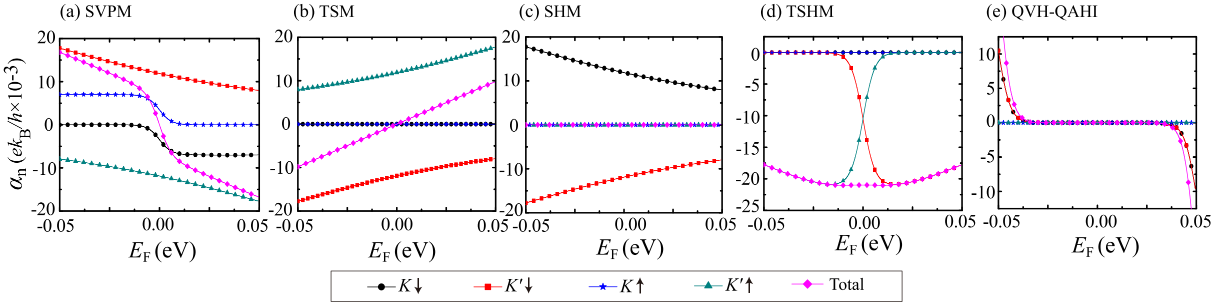

FIG. 7. Anomalous Nernst conductivity as a function of the Fermi level. The parameters in (a)–(e) correspond to those in the topological phases SVPM, TSM, SHM, TSHM, and QVH-QAHI in Figs. 3(b), 3(c) 3(e), 3(f), and 3(i).

opposite, but the bulk state with spin down contributes to the transport. The Nernst conductivity with spin up is zero, and the ones with spin down in different valleys are reversed; the total Nernst conductivity in Fig. 7(c) is zero, but spin-locked valley splitting can be achieved. For the single-valley TSHM, the state with spin up is a band insulator, while the state with spin down is a topological insulator. As plotted in Fig. 6(d), for the conduction band, the Berry curvatures with different spins at the K' valley are inverted. When the Fermi level locates near the zero energy, the contributions to the Nernst conductivity are from the electrons in the conduction band with spin down and the valence band with spin up. Hence, the Nernst conductivities are homodromous. Interestingly, the spins of the Nernst current are flipped as a function of the Fermi level, and the total Nernst conductivity are 100% spin and valley polarized when the absolute value of the Fermi level is large, which can be seen in Fig. 7(d). For the QVH-QAHI, the electrons referred to the anomalous Nernst conductivity are from the conduction or valence bands simultaneously. The sign of the Nernst conductivity is the same as the Berry curvature. As shown in Fig. 7(e), spin-locked K and K' valley electrons contribute to the Nernst conductivities, and the total Nernst conductivity is fully spin polarized. When the Fermi level is larger (smaller) than the zero energy, the Nernst conductivity is negative (positive). The spin and valley can be selected by changing the external fields. Moreover, it can be found although the signs of the Berry curvatures in the TSHM and QVH-QAHI are the same in Fig. 6, the anomalous transverse transport properties are very different due to the insulating or metallic bulk states.

V. EXTERNAL FIELD MODULATED SWITCH

As an application, for the specific band structure of the single-valley TSHM, we propose to realize an electrically or magnetically modulated switch with a two-terminal junction, which is schematically shown in Fig. 8(a). The junction is composed of TSHM1 and TSHM2, where the parameters of the external fields in regions I and II are different. The source-drain device can be driven by a temperature or electric bias. When the two parts of the junction are the same, the electrons can be transmitted obviously. The matched band structures are illustrated in Fig. 8(b) and the switch remains on state.

Three methods can be designed to obtain the off state by utilizing the TSHM flexibly. For the first one, one can attach a gate voltage on region II, and then the potential barrier of the height is V. Once the potential barrier $V > E_F$, the Fermi level (dashed line) lies in the conduction band outside the barrier and the valence band inside it. As a result of spin mismatching, the transmission is low (off state), which can be seen from Fig. 8(c). For the second one, without gate voltage, the off state can be realized by reversing the magnetization of the ferromagnetic substrates. The energy spectrum has the relation $E(\sigma, M) = E(-\sigma, -M)$. When the magnetization in region II $M_2 = -M_1$, the spins in the band exchange with each other, and the transmission is also blocked, which can be seen schematically in Fig. 8(d). At last, when the irradiation parameter in region II $\lambda_{\Omega 2} = -\lambda_{\Omega 1}$ by tuning the polarization of the off-resonant light, the other parameters have no change, $E(\eta, \lambda_\Omega) = E(-\eta, -\lambda_\Omega)$, and the bands at different valleys are exchanged, as shown in Fig. 8(e). Due to the valley mismatching, the electrons cannot be transmitted. By using of the special energy spectrum of the TSHM, the on-off state can be easily switched by tuning one of the external fields.

VI. CONCLUSIONS

In summary, we have investigated the various topological phases in irradiated graphene with asymmetric ferromagnetic fields. Particularly, we have concentrated on the often over-

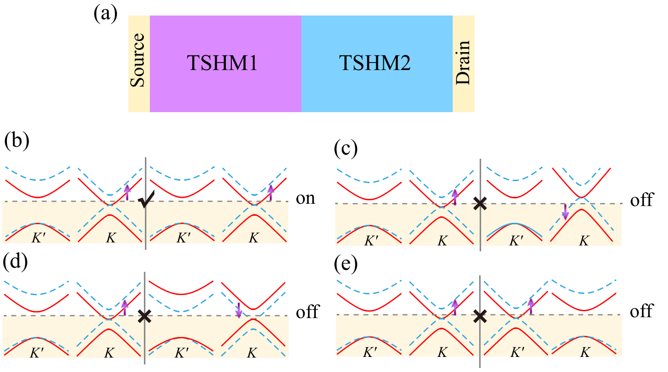

FIG. 8. (a) Schematic of a two-terminal device composed of TSHM1 and TSHM2 connecting to the source and drain as the ends. (b)–(e) Band alignments of the junction. (b) The parameters in the two regions of the junction are the same. (c) $M_1 = M_2$, $\lambda_{\Omega 1} = \lambda_{\Omega 2}$, the gate voltage in region II $V > E_F$. (d) $M_1 = -M_2$, $\lambda_{\Omega 1} = \lambda_{\Omega 2}$. (e) $M_1 = M_2$, $\lambda_{\Omega 1} = -\lambda_{\Omega 2}$. Dashed lines denote the Fermi levels; the energy at the Dirac cone is set as the zero energy level. The on (off) state represents that the electrons can be transmitted (blocked).

looked topological properties of some special metal phases, which are the SVPM, SHM, TSM, and TSHM. Different from the traditional metal, the Berry curvatures in the topological metal phases are found to be nonzero. Because the disappearing topological edge states in nanoribbons and ill-defined Chern numbers make it difficult to characterize the topological properties of a metal state, we study the anomalous Nernst effect to distinguish them. The deflection of the Nernst currents depends on the sign of the Berry curvature and the bulk states of the metal phases. Furthermore, in this system, valley-resolved spin splitting and flip, and spin-resolved valley splitting, can be obtained. By utilizing some peculiar topological phases, we have designed an electrically or magnetically controlled on/off switch. These findings provide another view to control the transport properties of spin and valley in graphene with a specific metallic state, and they are expected to be applied in future spin-valley caloritronics.

ACKNOWLEDGMENTS

This work was supported by the National Natural Science Foundation of China (Grants No. 11747019, No. 11804291, and No. 12074156), the Natural Science Foundation of Jiangsu Province (Grant No. BK20180890), the Universities Natural Science Research Project of Jiangsu Province (Grant No. 17KJB140031), and the Yunnan Local Colleges Applied Basic Research Projects (Grant No. 2017FH001-001).

[1] K. S. Novoselov, A. K. Geim, S. V. Morozov, D. Jiang, Y. Zhang, S. V. Dubonos, I. V. Grigorieva, and A. A. Firsov, Science **306**, 666 (2004).
[2] A. H. Castro Neto, F. Guinea, N. M. R. Peres, K. S. Novoselov, and A. K. Geim, Rev. Mod. Phys. **81**, 109 (2009).
[3] C. L. Kane and E. J. Mele, Phys. Rev. Lett. **95**, 226801 (2005).
[4] S. Das Sarma, S. Adam, E. H. Hwang, and E. Rossi, Rev. Mod. Phys. **83**, 407 (2011).
[5] R. C. Andrew, R. E. Mapasha, A. M. Ukpong, and N. Chetty, Phys. Rev. B **85**, 125428 (2012).
[6] A. Avsar, H. Ochoa, F. Guinea, B. Özyilmaz, B. J. van Wees, and I. J. Vera-Marun, Rev. Mod. Phys. **92**, 021003 (2020).
[7] C.-C. Liu, W. Feng, and Y. Yao, Phys. Rev. Lett. **107**, 076802 (2011).
[8] T. Cao, G. Wang, W. Han, H. Ye, C. Zhu, J. Shi, Q. Niu, P. Tan, E. Wang, B. Liu, and J. Feng, Nat. Commun. **3**, 887 (2012).
[9] G. Fiori, F. Bonaccorso, G. Iannaccone, T. Palacios, D. Neumaier, A. Seabaugh, S. K. Banerjee, and L. Colombo, Nat. Nanotechnol. **9**, 768 (2014).
[10] M. Ezawa, J. Phys. Soc. Jpn. **84**, 121003 (2015).
[11] L. Tao, E. Cinquanta, D. Chiappe, C. Grazianetti, M. Franciulli, M. Dubey, A. Molle, and D. Akinwande, Nat. Nanotechnol. **10**, 227 (2015).
[12] Z. Qin, J. Pan, S. Lu, Y. Shao, Y. Wang, S. Du, H.-J. Gao, and G. Cao, Adv. Mater. **29**, 1606046 (2017).
[13] A. Hoffmann and S. D. Bader, Phys. Rev. Appl. **4**, 047001 (2015).
[14] X. Chen, Y. Liu, B. L. Gu, W. Duan, and F. Liu, Phys. Rev. B **90**, 121403(R) (2014).
[15] Z. P. Niu, New J. Phys. **20**, 103021 (2018).
[16] S. A. Vitale, D. Nezich, J. O. Varghese, P. Kim, N. Gedik, P. Jarillo-Herrero, D. Xiao, and M. Rothschild, Small **14**, 1801483 (2018).
[17] M. Ezawa, Phys. Rev. B **87**, 155415 (2013).
[18] M. Ezawa, Phys. Rev. Lett. **109**, 055502 (2012).
[19] M. Ezawa, Phys. Rev. Lett. **110**, 026603 (2013).
[20] D. Xiao, M.-C. Chang, and Q. Niu, Rev. Mod. Phys. **82**, 1959 (2010).
[21] D. N. Sheng, Z. Y. Weng, L. Sheng, and F. D. M. Haldane, Phys. Rev. Lett. **97**, 036808 (2006).
[22] E. Prodan, Phys. Rev. B **80**, 125327 (2009).
[23] D. Xiao, Y. Yao, Z. Fang, and Q. Niu, Phys. Rev. Lett. **97**, 026603 (2006).
[24] X. Zhou, Y. Xu, and G. Jin, Phys. Rev. B **92**, 235436 (2015).
[25] Y. Xu, X. Zhou, and G. Jin, Appl. Phys. Lett. **108**, 203104 (2016).
[26] X. Zhai, S. Zhang, Y. Zhao, X. Zhang, and Z. Yang, Appl. Phys. Lett. **109**, 122404 (2016).
[27] X. Zhai, Y.-T. Wang, R. Wen, S.-X. Wang, Y. Tian, X. Zhou, W. Chen, and Z. Yang, Phys. Rev. B **97**, 085410 (2018).
[28] J. C. Leutenantsmeyer, A. A. Kaverzin, M. Wojtaszek, and B. J. van Wees, 2D Mater. **4**, 014001 (2017).
[29] J. R. Schaibley, P. Rivera, H. Yu, K. L. Seyler, J. Yan, D. G. Mandrus, T. Taniguchi, K. Watanabe, W. Yao, and X. Xu, Nat. Commun. **7**, 13747 (2016).
[30] S. Tang, H. Wang, Y. Zhang, A. Li, H. Xie, X. Liu, L. Liu, T. Li, F. Huang, X. Xie, and M. Jiang, Sci. Rep. **3**, 2666 (2013).
[31] M. Yankowitz, J. Xue, D. Cormode, J. D. Sanchez-Yamagishi, K. Watanabe, T. Taniguchi, P. Jarillo-Herrero, P. Jacquod, and B. J. LeRoy, Nat. Phys. **8**, 382 (2012).
[32] T. Kitagawa, T. Oka, A. Brataas, L. Fu, and E. Demler, Phys. Rev. B **84**, 235108 (2011).
[33] X. Li, T. Cao, Q. Niu, J. Shi, and J. Feng, Proc. Natl. Acad. Sci. USA **110**, 3738 (2013).
[34] P. Wei, S. Lee, F. Lemaitre, L. Pinel, D. Cutaia, W. Cha, F. Katmis, Y. Zhu, D. Heiman, J. Hone, J. S. Moodera, and C.-T. Chen, Nat. Mater. **15**, 711 (2016).
[35] A. Dyrdał and J. Barnaś, 2D Mater. **4**, 034003 (2017).
[36] X.-L. Lü and H. Xie, New J. Phys. **22**, 073003 (2020).
[37] T. Mikami, S. Kitamura, K. Yasuda, N. Tsuji, T. Oka, and H. Aoki, Phys. Rev. B **93**, 144307 (2016).
[38] F. D. M. Haldane, Phys. Rev. Lett. **61**, 2015 (1988).
[39] O. V. Kibis, K. Dini, I. V. Iorsh, and I. A. Shelykh, Phys. Rev. B **95**, 125401 (2017).
[40] G. Giovannetti, P. A. Khomyakov, G. Brocks, P. J. Kelly, and J. van den Brink, Phys. Rev. B **76**, 073103 (2007).
[41] C. R. Dean, A. F. Young, I. Meric, C. Lee, L. Wang, S. Sorgenfrei, K. Watanabe, T. Taniguchi, P. Kim, K. L. Shepard, and J. Hone, Nat. Nanotechnol. **5**, 722 (2010).
[42] S. Y. Zhou, G.-H. Gweon, A. V. Fedorov, P. N. First, W. A. de Heer, D.-H. Lee, F. Guinea, A. H. Castro Neto, and A. Lanzara, Nat. Mater. **6**, 770 (2007).

[43] S. Wang, P. Zhang, C. Ren, H. Tian, J. Pang, C. Song, and M. Sun, J. Supercond. Novel Magn. **32**, 2947 (2019).

[44] K. Ando and E. Saitoh, Nat. Commun. **3**, 629 (2012).

[45] M. Yamamoto, Y. Shimazaki, I. V. Borzenets, and S. Tarucha, J. Phys. Soc. Jpn. **84**, 121006 (2015).

[46] Y. Shimazaki, M. Yamamoto, I. V. Borzenets, K. Watanabe, T. Taniguchi, and S. Tarucha, Nat. Phys. **11**, 1032 (2015).